MOLECULAR IMAGING AND BIOLOGY

Published Online: 21 November 2009

Mol Imaging Biol (2010) 12:394–405
DOI: 10.1007/s11307-009-0288-y

RESEARCH ARTICLE

Fluorescence Imaging and Whole-Body Biodistribution of Near-Infrared-Emitting Quantum Dots after Subcutaneous Injection for Regional Lymph Node Mapping in Mice

Emilie Pic,[1] Thomas Pons,[2] Lina Bezdetnaya,[1] Agnès Leroux,[3] François Guillemin,[1] Benoît Dubertret,[2] Frédéric Marchal[1]

[1]*Centre de Recherche en Automatique de Nancy—Nancy-University—CNRS—Centre Alexis Vautrin, avenue de Bourgogne, 54511, Vandoeuvre-lès-Nancy Cedex, France*
[2]*Laboratoire Photons et Matière, CNRS UPRA0005, ESPCI, 10 rue Vauquelin, 75005, Paris, France*
[3]*Department of Pathology, Centre Alexis Vautrin, avenue de Bourgogne, 54511, Vandoeuvre-lès-Nancy Cedex, France*

Abstract

Purpose: This study compares fluorescence imaging to mass spectroscopy (inductively coupled plasma–mass spectroscopy, ICP–MS) for detection of quantum dots (QDs) in sentinel lymph node (LN) mapping of breast cancer.

Procedures: We study the accumulation of near-infrared-emitting QDs into regional LNs and their whole-body biodistribution in mice after subcutaneous injection, using *in vivo* fluorescence imaging and *ex vivo* elemental analysis by ICP–MS.

Results: We show that the QD accumulation in regional LNs is detectable by fluorescence imaging as early as 5 min post-delivery. Their concentration reaches a maximum at 4 h then decreases over a 10-day observation period. These data are confirmed by ICP–MS. The QD uptake in other organs, assessed by ICP–MS, increases steadily over time; however, its overall level remains rather low.

Conclusions: Fluorescence imaging can be used as a non-invasive alternative to ICP–MS to follow the QD accumulation kinetics into regional LNs.

Key words: Quantum dots, Lymph nodes, Near-infrared fluorescence imaging, Mass spectroscopy, Biodistribution

Abbreviations: % ID, Percentage of injected dose; Abs, Absorbance; ALN, Axillary lymph node; ALND, Axillary lymph node dissection; AU, Arbitrary unit; DLS, Dynamic light scattering; DPPE, Dipalmitoyl phosphotidylethanolamine; H&E, Hematoxylin and eosin; HD, Hydrodynamic diameter; ICP–AES, Inductively coupled plasma–atomic emission spectroscopy; ICP–MS, Inductively coupled plasma–mass spectroscopy; i.v., Intravenous; LALN, Left axillary lymph node; LED, Light-emitting diode; LLTLN, Left lateral thoracic lymph node; LN, Lymph node; LTLN, Lateral thoracic lymph node; Me, Methyl ether; microPET, Micro-positron emission tomography; NIR, Near-infrared; PBS, Phosphate buffered saline; PEG, Polyethylene glycol; PL, Photoluminescence; QD, Quantum dot; RALN, Right axillary lymph node; RLTLN, Right lateral

Manuscript category and significance The present "research article" addresses near-infrared-emitting quantum dots detection by fluorescence imaging as a non-invasive and reliable method for identification of regional lymph nodes for their eventual use in breast tumor patients.

Correspondence to: Frédéric Marchal; *e-mail:* f.marchal@nancy.fnclcc.fr

thoracic lymph node; ROI, Region of interest; s.c., Subcutaneous; SD, Standard deviation; SLN, Sentinel lymph node; SLNB, Sentinel lymph node biopsy; TEM, Transmission electron microscopy; TOP, Trioctylphosphine

Introduction

Axillary lymph node (ALN) status is the most important prognostic factor in patients with breast cancer and a determinant predictor of recurrence and survival [1, 2]. Until recently, the standard surgical treatment in breast cancer was axillary lymph node dissection (ALND), which consists in whole lymphatic axillary chain removal, but leads to numerous postoperative morbidities, deteriorating the quality of life. For these reasons, sentinel lymph node biopsy (SLNB) has become the new standard method of staging breast cancer patients [3]. The sentinel lymph node (SLN) is the first regional step of lymphatic drainage and metastasis of the primary tumor [1, 4]. SLNB allows to identify sentinel ALN and involves the use of technetium sulfur colloid and isosulfan blue dye in the USA, and technetium-labeled albumin and patent blue dye in EU countries. The combined use of radiocolloid and blue dye increases recognition of the SLNs [2, 5]. The day before surgery, the radiocolloid is injected, many routes of injection being used (peritumoral, intratumoral, subcutaneous, intradermal, or subareolar), followed by mammary and axillary lymphoscintigraphy between 30 min and 4 h post-administration. During the surgery, a mean volume of 3–4 mL of blue dye is delivered by the same way, and SLNs are identified as blue and/or hot lymph nodes (LNs) [6, 7]. Despite the significant improvement of SLNB over ALDN, the problems related to an extra cost of the radioisotope, to allergic reactions and in a few cases anaphylactic shocks after radiocolloid or blue dye injection, and the overall procedure duration are limiting factors for this technique [8–11]. Moreover, lymphatic mapping with blue dye results in a high rate of false-positive nodes because the small dye molecules can readily diffuse through the true SLN and traverse multiple nodes [12]. Additionally, blue dye has poor tissue contrast and is difficult to detect in deep, dark anatomical regions such as the abdomen. Although the use of radioisotope tracers has improved the detection rate and accuracy of SLN mapping, the high radioactivity of the primary injection site can interfere with intraoperative *in vivo* detection of nearby nodes [1].

Near-infrared (NIR) fluorescence imaging appears as a promising alternative for SLN mapping due to its flexibility, non-invasive procedure, high temporal resolution, and low cost. In particular, semiconductor quantum dots (QDs) are promising candidates for NIR imaging probes for this application thanks to their unique optical and physical properties, namely optimal physical size, high fluorescent quantum yield, large molar extinction coefficient, and particularly high resistance to photobleaching [13–15], that alleviate many of the common organic dye limitations. QDs are composed of a nanometer-scale fluorescent semiconductor core such as the most common CdSe or CdTe. These cores can be overcoated with a first inorganic shell (e.g., ZnS) to improve their photoluminescence quantum yields and limit their potential toxicity due to the release of toxic core heavy metal ions [16, 17]. These core–shell QDs are solubilized in water by cap exchange with appropriate surface ligands or encapsulation by amphiphilic block co-polymers or functionalized lipids [18–20]. Control over this surface chemistry is crucial as it will determine the fate of the QDs in a biological environment (cell, tissue, organism…).

NIR-emitting QDs have already been applied to visualize SLN in gastrointestinal tract [21], pleural space [22], lung area [23], esophageal area [24], skin [25], axilla [26–29], and bladder area [30] in rodents and pigs. The authors have performed fluorescence imaging of LNs for up to 4 h after QD injection; however, the long-term QD biodistribution was not investigated after subcutaneous injection. Understanding and controlling the QD biodistribution is of the utmost importance in biomedical applications as it will impact the imaging performance (rapidity, sensitivity, specificity) and the potential QD toxicity. In particular, in the case of SLN detection, both the peritumoral injection site and the SLNs would be resected, and the toxicity would depend on the proportion of QDs leaking into the rest of the organism. In the present paper, we study the QD accumulation kinetics in regional LNs and the whole-body biodistribution of lipid-encapsulated QDs in mice for up to 10 days after subcutaneous (s.c.) injection of NIR carboxyl-functionalized lipid coated QDs. We use both NIR fluorescence, the modality which would be used *in fine* during the surgical act, and inductively coupled plasma–mass spectroscopy (ICP–MS), which provides quantitative measurements of QD concentration [31–40]. We demonstrate that NIR imaging allows a fast and sensitive detection of regional LNs with QDs. We further evaluate the reliability of NIR imaging measurements by comparison with quantitative ICP–MS elemental analysis. The obtained results provide useful indications for optimization of the surgical procedure to allow efficient regional LN detection.

Materials and Methods

Near-Infrared-Emitting Quantum Dot Synthesis

CdTeSe/CdZnS core/shell QDs were synthesized following a recently published protocol [20]. Briefly, CdTeSe cores were

synthesized by injection of trioctylphosphine (TOP)–Se and TOPTe in a three-neck flask containing Cd-tetradecylphosphonate, TOP, and oleylamine at 280°C. The solution was then kept at 230°C, and additional TOPSe precursors were injected by dropwise injection. A CdZnS shell was grown over the CdTeSe cores by injection of TOP-S in a solution of trioctylamine, TOP, Cd-oleate and Zn-oleate. These CdTeSe/CdZnS QDs were characterized by absorbance and photoluminescence spectroscopy using a Cary-5E UV–vis spectrophotometer (Varian) and Fluoromax-3 fluorimeter (Jobin Yvon, Horiba). Transmission electron microscopy (TEM) images were acquired on a JEOL 2010 field electron gun microscope.

Quantum Dot Solubilization

CdTeSe/CdZnS nanocrystals were solubilized by encapsulation into functionalized amphiphilic phospholipid micelles, as described previously [19, 20, 41]. Typically, the core/shell QDs were washed with two cycles of precipitation in ethanol and resuspension in hexane, and finally resuspended in chloroform with a mixture of 66% DPPE-PEG2000-Me (dipalmitoyl phosphotidylethanolamine-polyethylene glycol 2000-methyl ether) and 33% DPPE-PEG2000-COOH (dipalmitoyl phosphotidylethanolaminepolyethylene glycol 2000-carboxylic acid) and deionized water. The chloroform was evaporated by heating at 80°C, yielding a limpid solution. These water-soluble QDs were then purified by ultracentrifugation following previously published protocols [19, 41] to remove excess lipids and small QD aggregates. Stock QD solutions were stored at 4°C before use. Dynamic light scattering measurements were performed on a CGS-3 goniometer system equipped with a HeNe laser illumination at 633 nm (Malvern) and an ALV 5000/EPP correlator (ALV). Electrophoresis was run in 2% agarose gel in a Tris–borate–EDTA pH 8 buffer.

Animals

Ten- to twelve-week-old female balb/c mice (Balb/cOlaHsd; Harlan, Gannat, France) weighing from 18 to 22 g were used in these experiments. Mice were kept in a 12-h light/dark cycle and had access to food and water *ad libitum*. The mice were acclimated for 2 weeks prior to use. Specific purified diet (TD.94045, Harlan Teklad, Madison, WI, USA) was used to reduce tissue autofluorescence in the NIR spectral region. The animals received care in accordance with established guidelines of the Federation of European Laboratory Animal Science Associations, and animal procedures were performed in compliance with institutional and national guidelines. All experiments were performed under anesthetic using intraperitoneal injection of 0.01 mL/g of body weight of a solution containing 9 mg/mL of ketamine (Ketalar®, Panpharma, Fougères, France) and 0.9 mg/mL of xylazine (Rompun®, Bayer Pharma, Puteaux, France). Control mice were injected subcutaneously in the distal part of the right anterior paw with 20 µL of phosphate buffered saline (PBS), and for experimental groups, 20 µL of a 1-µM QD solution (20 pmol) was administered in the same way. After product delivery, the right paw was kneaded to improve product migration.

Near-Infrared Fluorescence Imaging

In vivo optical imaging of QDs was performed using a Fluobeam® (Fluoptics, Grenoble, France) NIR imaging system. This system is compact and portable, and is composed of two principle parts (Fig. 1a). The first part is an electric panel box including a laser emitting at 690 nm and its power supply, an analogical/digital box, and a power supply for light-emitting diodes (LEDs). The second part is the optical head containing a highly sensitive charge-coupled device (CCD) camera and white LEDs (Fig. 1a, b). From the electric box, the laser beam is guided by a fiber until the extremity of the optical head, thus rendering possible the divergence of the optical system and excitation of a broad field of about 6 cm in diameter to the distance of 15 cm from the extremity of optical head. A 750-nm longpass emission filter is used. The power density of laser irradiation on tissue was 3 mW/cm^2. For semi-quantitative *in vivo* fluorescence measurements, the optical head is supported by a hinged jib and was kept at the same place during the experimental period (Fig. 1b). The regions of interest (ROIs) were depilated using a commercial hair removal cream before imaging. Three mice were injected subcutaneously with QDs and three control mice were injected with PBS. The CCD camera shows the specificity to adjust the fluorescence signal on the pixel which presents the strongest fluorescence intensity. Thus, the injection

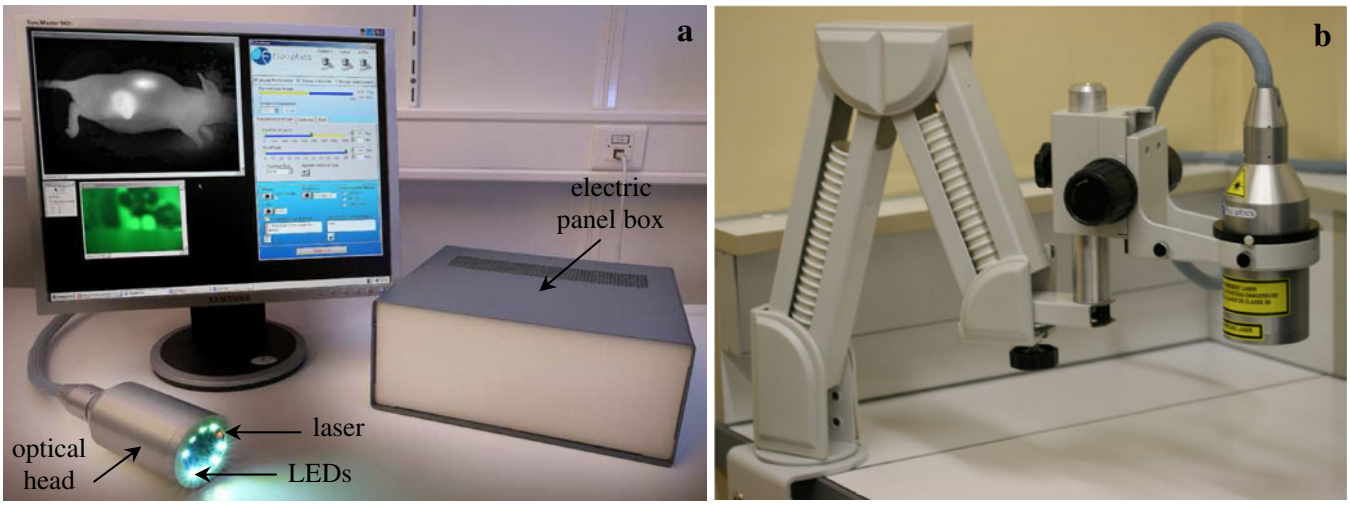

Fig. 1. Photographs of portable and compact Fluobeam® system. **a** Composition of Fluobeam® system. **b** Image of optical head supported by a hinged jib to carry out semi-quantitative fluorescence imaging *in vivo*.

point of QDs was hidden, allowing thereby a better ROI visualization. *In vivo* fluorescence of ALNs and lateral thoracic LNs (LTLNs) was acquired at 5, 15, 30, and 60 min; 4, 24, 48, 96 h and 10 days after s.c. QD administration at a camera exposure time of 10 ms for right LNs and 100 ms for left LNs. Ten days after delivery of QDs or PBS, mice were sacrificed and *ex vivo* fluorescence signals of organs (ALNs, LTLNs, spleen, kidneys, liver, lungs, and brain) were measured after an exposure time of 100 ms. Semi-quantitative data can be obtained from the fluorescent images by drawing ROIs around the different organs to be quantified, and background signal (autofluorescence of tissues) is subtracted from all images. *In vivo* or *ex vivo* fluorescent signals were expressed in arbitrary units (AU) using the Image J 1.37 software. All images were acquired under the same conditions and were comparable from day to day and animal to animal. All data are represented as mean ± standard deviation (SD).

Inductively Coupled Plasma–Mass Spectroscopy (ICP–MS)

A Varian 820 MS instrument (Varian, Les Ulis, France) was used to perform ICP–MS analyses. All samples (organs, blood fractions, and excretions) were completely dissolved with 70% HNO_3 and heated at 90°C until total mineralization. Each mineralized sample was solubilized in 25 mL of milli-q water (resistivity >18.2 MΩ) and analyzed by ICP–MS at the Laboratoire Environnement-Hygiène of ASCAL (Forbach, France). The ICP–MS instrument was initialized, optimized, and standardized using manufacturer recommendations. The limit of cadmium quantification was 50 ng/mL. Five samples of 1 mL QD solutions at 20 nM (20 pmol) have been analyzed in the same conditions, previously described, to correlate cadmium and QD concentrations. Ten groups of animals (n=3 per group) were used for the biodistribution study: one control group received PBS and nine experimental groups were injected with QDs. Sacrifice of control group was performed 10 days after PBS injection and experimental groups were sacrificed at 5, 15, 30, and 60 min; 4, 24, 48, 96 h and 10 days after QD injection by cervical dislocation. ALNs, LTLNs, spleen, kidneys, liver, lungs, brain, and injection point defined as the distal part of the right anterior paw were removed and their weights were recorded. Blood samples were collected through cardiac puncture in heparinized tubes at the different times after QD injection. Blood samples were centrifuged at 3,000×*g* for 10 min to separate plasma and blood cells. Urine and feces were collected daily during 10 days. All removed samples were stored at −80°C prior to elemental analysis. All data are represented as mean ± SD.

Histology of Lymph Node Section

Two groups of animals (n=3 per group) were used for histological study of ALNs and LTLNs. Animals were sacrificed 10 days after QD or PBS injection by cervical dislocation. ALNs and LTLNs were removed for histological analysis. All tissues were fixed in 10% formaldehyde, 5-µm sections of LNs were prepared, and hematoxylin and eosin (H&E) coloration was performed and examined to visualize inflammatory changes.

Statistical Calculations

Means, SD, correlation coefficients, and statistical significance of differences between groups (Student's t test) were determined using standard software (Microsoft Excel, Microsoft Corporation, Redmond, WA, USA); p values <0.05 were considered statistically significant.

Results

QD Synthesis and Characterization

We synthesized NIR-emitting QDs composed of CdTeSe cores surrounded by a CdZnS shell [20] with ~6 nm in core–shell diameter. Absorbance (Abs) and photoluminescence (PL) spectra of these QDs are shown in Fig. 2a, with an emission maximum at around 780 nm. The QDs were solubilized in water by encapsulation into phospholipid

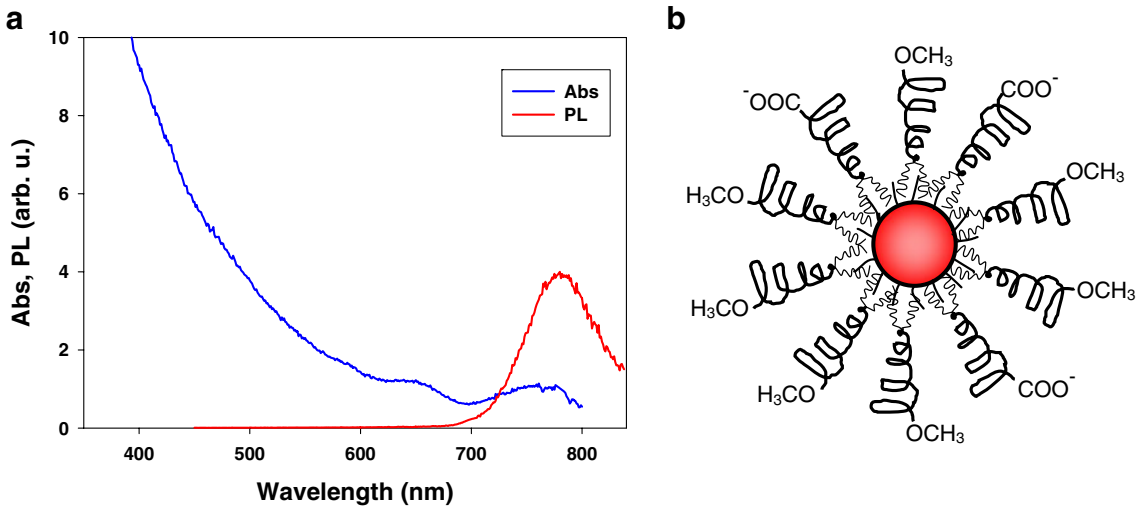

Fig. 2. **a** Absorbance (*Abs*) and photoluminescence (*PL*) emission spectra of CdTeSe/CdZnS QDs. **b** Schematics representing a CdTeSe/CdZnS QD encapsulated in a mixed PEG:PEG-COOH phospholipid micelle (drawing is not to scale; only a few phospholipids were represented for clarity).

micelles functionalized with 66% polyethylene glycol (PEG) 2000 and 33% PEG2000-carboxylic acid (COOH), as shown by the schematic in Fig. 2b [19, 41]. The carboxylic acid groups confer a negative electric charge to the QD surface, as indicated by migration under gel electrophoresis. Hydrodynamic diameters (HD) of the QDs micelles are typically ~22 nm, as indicated by dynamic light scattering (DLS). The QD fluorescence quantum yield was typically ~20–30% after solubilization, and was stable for several weeks in neutral (PBS, pH 7) or slightly basic (borate, pH 8) buffer, and at least several days in slightly acidic PBS (pH 6) buffer [20].

Near-Infrared Fluorescence Imaging

In vivo imaging Twenty picomoles of QDs were injected subcutaneously in the distal part of the right anterior paw. Right ALN (RALN) and right lateral thoracic LN (RLTLN) are visualized as early as 5 min after injection and for the whole 10-day observation period, while only background

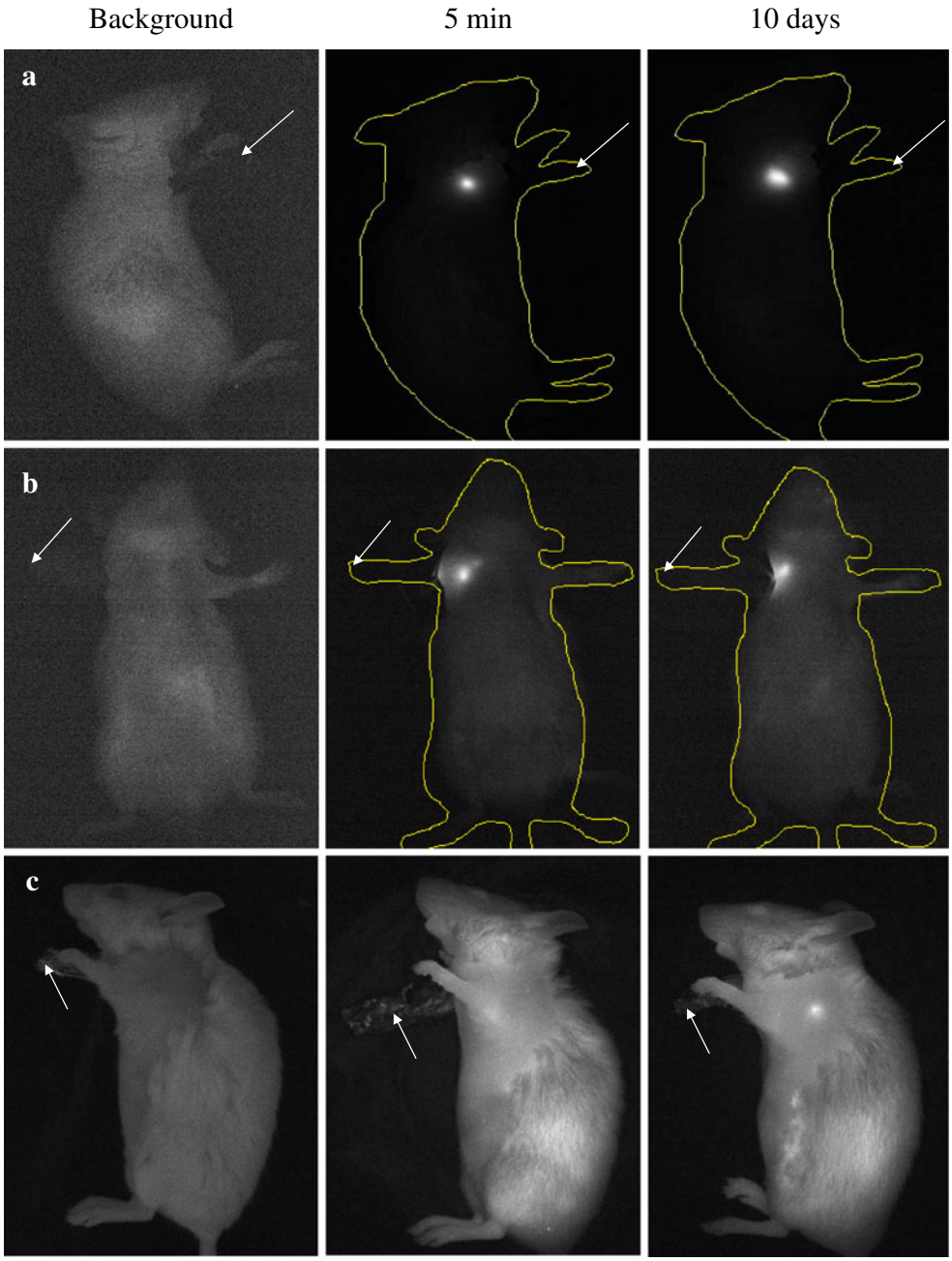

Fig. 3. *In vivo* fluorescence imaging of mice after s.c. injection of 20 pmol of QDs. **a** Images of the right flank (visualization of RALN). **b** Images on dorsal decubitus (observation of RLTLN). **c** Images of left flank (visualization of LALN). *Left column* corresponds to background signal, *middle* and *right columns* to images at 5 min and 10 days post-injection, respectively. For (**a**) and (**b**) images, the exposure time is 10 ms, and for (**c**) images, the exposure time is 100 ms. The *white arrow* indicates the injection point.

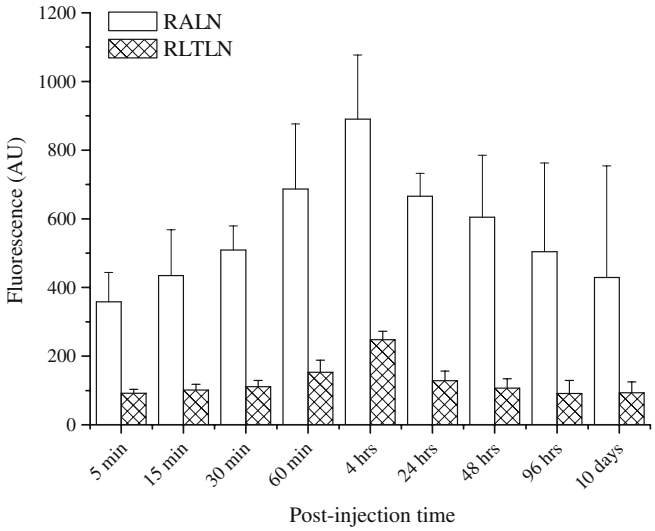

Fig. 4. *In vivo* fluorescence signals of QDs in RALN and RLTLN after s.c. injection of 20 pmol in mice functions of time. For fluorescence analyses of images, the exposure time is 10 ms. Data are mean ± SD (n=3).

signal was observed in control QD-free mice (Fig. 3). Figure 3 displays the NIR images taken at selected points: right flank (Fig. 3a), dorsal decubitus (Fig. 3b), and left flank (Fig. 3c) to visualize RALN, LTLN, and left ALN (LALN), respectively. Detailed kinetics of fluorescence intensities are presented in Fig. 4. Intensity of fluorescence signals in RALN and RLTLN increases during the first 4 h post-injection, then gradually decreases for the rest of the observation period (Fig. 4). Fluorescence from the LALN is visualized 24 h after QD delivery in two out of three mice, but its signal is much weaker and cannot be quantified due to low signal-to-background ratio (Fig. 3c).

Ex vivo imaging QDs were detected *ex vivo* in four resected LNs 10 days after s.c. administration (Fig. 5a). A strong *ex vivo* fluorescence intensity is observed in RALN and RLTLN compared to LALN and left LTLN (LLTLN) 10 days post-QD injection (Fig. 5b, c). Indeed, fluorescence signal in RALN is 260-fold greater compared to LALN (Fig. 5b, c) and 160-fold more elevated in RLTLN than that in LLTLN (Fig. 5b, c). No difference in fluorescence signals was detected in other organs compared to control mice (data not shown).

Biodistribution Study by ICP–MS

We injected 20 pmol of QDs subcutaneously in the right anterior paw of mice and monitored accumulation kinetics between 5 min and 10 days after administration. Major organs, blood, and excretions were collected at all experimental times and analyzed by ICP–MS to determine cadmium concentration (Fig. 6). Percentage of injected doses (% ID) were then estimated using prior calibration of our QD sample (20 nM QDs corresponded to 685±4 μM of cadmium; Fig. 7).

The remaining cadmium at the site of injection, defined as the distal part of the right anterior paw, is shown in Figs. 6a and 7a. Cadmium concentrations remain constant between 5 and 60 min corresponding to a loss of approximately 60% ID from the injection site. Given the cadmium concentrations measured from the rest of the organs and the blood, this loss is due to QD diffusion into the tissue in the immediate vicinity of the injection site corresponding to the whole right paw and the right shoulder. After 60 min, the cadmium concentration decreases steadily during the next 10 days. At the end of this observation period, the cadmium concentration reaches 33.41±2.14 μg/g, corresponding to 14.63±1.96% ID (Figs. 6a and 7a).

QDs are readily detected in RALN and RLTLN as early as 5 min after their administration, and the corresponding cadmium concentration increases. Maximum cadmium concentrations in RALN and RLTLN are observed at 4 h post-injection (337.8±50.3 μg/g and 283.6±8.1 μg/g, corresponding to 1.36±0.21% ID and 0.94±0.13% ID, respectively; Figs. 6a and 7b). Cadmium concentrations then progressively decrease for the rest of the 10-day observation period. However, the % ID remains constant in these nodes between 4 h and 10 days post-delivery (Fig. 7b). It is important to note that mass spectroscopy, in terms of

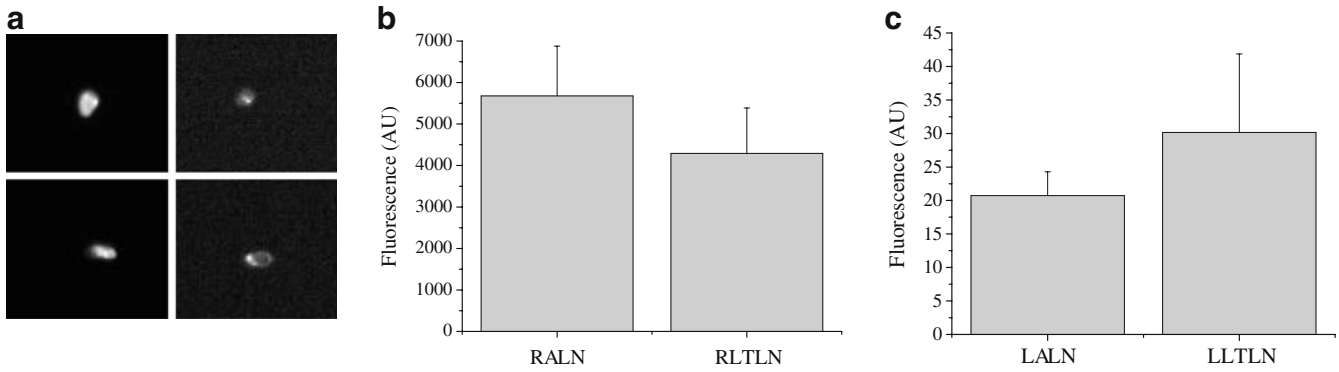

Fig. 5. *Ex vivo* fluorescence signals of four removed LNs. Mice were subcutaneously injected with 20 pmol of QDs and sacrificed at 10 days. **a** Fluorescence images of LNs: RALN (*upper left*), RLTLN (*lower left*), LALN (*upper right*), and LLTLN (*lower right*). **b** Relative fluorescence signal of right LNs (*RALN* and *RLTLN*) and **c** left LNs (*LALN* and *LLTLN*). For fluorescence measurements, the exposure time is 100 ms. Data are mean ± SD (n=3).

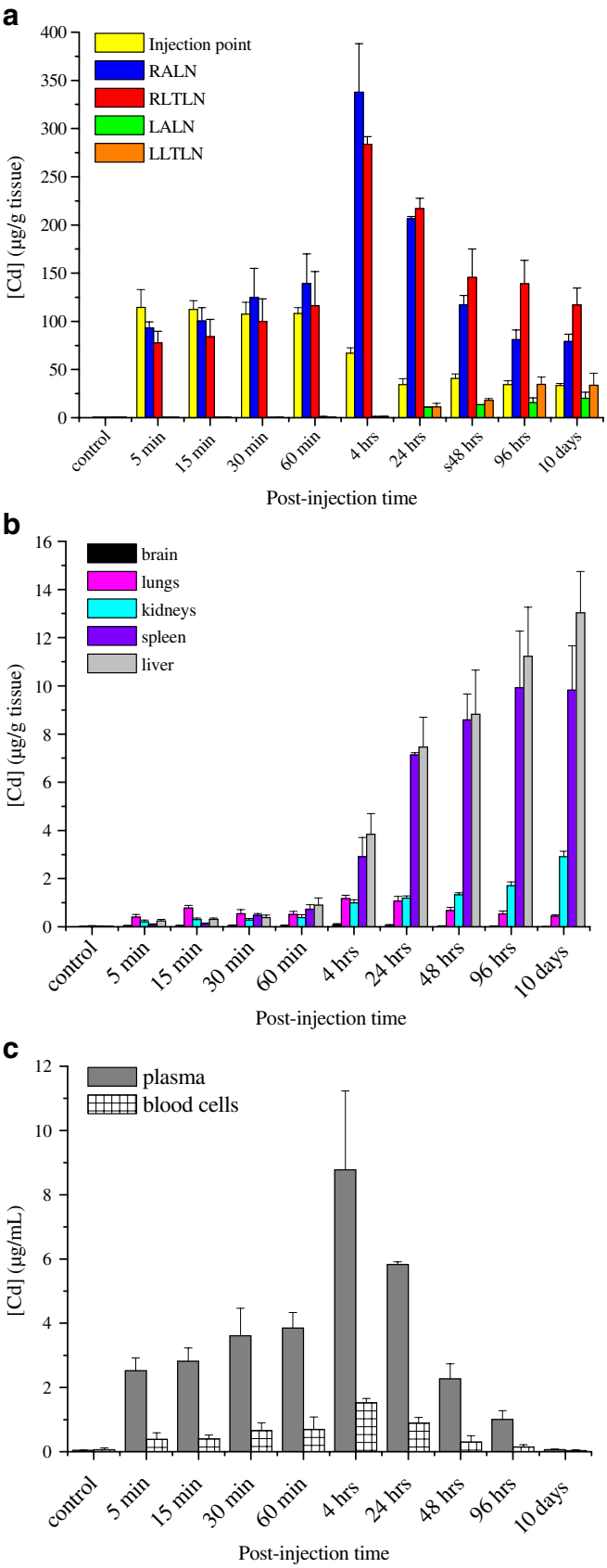

◀ **Fig. 6.** Tissue kinetics of cadmium concentrations in mice after s.c. administration. Mice were injected with 20 pmol of QDs or PBS (control). Serial sacrifices were carried out at 5, 15, 30, and 60 min at 4, 24, 48, and 96 h and at 10 days after dosing. Several organs were isolated to determine cadmium concentrations by ICP–MS: **a** injection point, RALN, RLTLN, LALN, and LLTLN; **b** brain, lungs, kidneys, spleen, and liver; **c** plasma and blood cells. Data are mean ± SD (n=3 per group).

cadmium concentration (Fig. 6a), and NIR fluorescence profiles of QDs into RALN and RLTLN (Fig. 4) are strictly similar. Statistical analyses demonstrate a strong correlation between these two detection techniques with a correlation coefficient of 0.89 (p<0.01) and 0.81 (p<0.01) for RALN and RLTLN, respectively (Fig. 8).

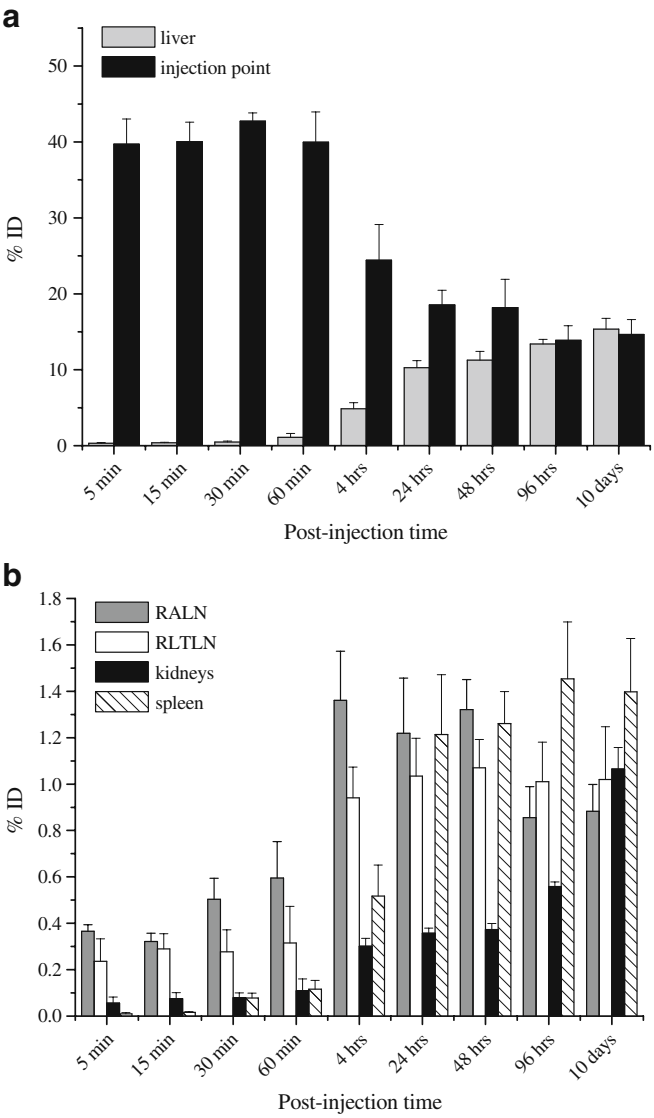

Fig. 7. Percentage of injected dose (*% ID*) in organs which most accumulate QDs. Mice were injected subcutaneously with 20 pmol of QDs. Serial sacrifices were carried out at 5, 15, 30, and 60 min at 4, 24, 48, and 96 h and at 10 days, and cadmium concentrations were measured. Several organs are represented: **a** liver and injection point; **b** RALN, RLTLN, kidneys, and spleen. Data are mean ± SD (n=3 per group).

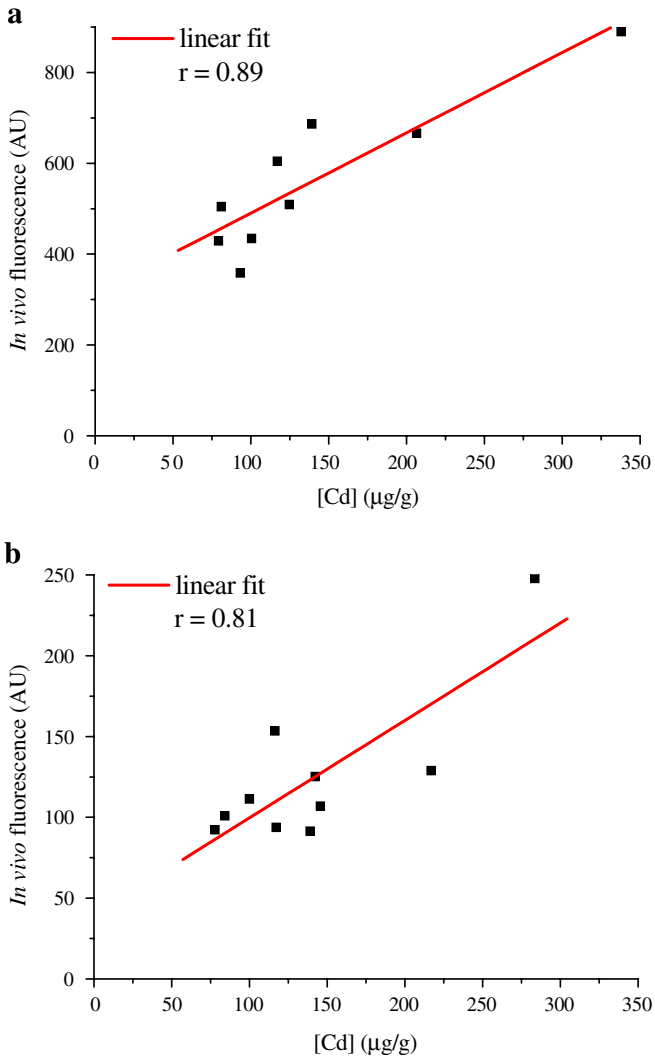

Fig. 8. Linear regression analyses and correlation coefficient values between cadmium concentrations measured by ICP–MS and *in vivo* fluorescence signals assessed by Fluobeam® system for RALN (**a**) and RLTLN (**b**).

In LALN and LLTLN, cadmium concentrations are much weaker and are detectable only after 4 h post-injection, then gradually increase for up to 10 days (Fig. 6a).

Kidneys, spleen, and liver display a progressive, time-dependent QD accumulation during the whole observation period (Figs. 6b and 7b). Ten days after QD injection, 2.91±0.22 (1.06±0.09% ID), 9.82±1.84 (1.40±0.24% ID), and 13.03±1.71 µg/g (15.36±1.39% ID) were found in kidneys, spleen, and liver, respectively. By contrast, brain and lungs show a different QD accumulation profile with much lower QD concentrations (Fig. 6b).

In blood, cadmium is detected as early as 5 min after QD administration and reaches a maximum at 4 h, corresponding to 8.78±2.46 µg/mL for plasma and 1.52±0.13 µg/mL for blood cells. Cadmium concentrations then progressively decrease with time to reach background levels at 10 days post-injection (Fig. 6c).

Urine and feces were collected daily but no QD excretion was detected during 10 days (data not shown).

Morphology and Histology of Lymph Nodes

The weights of the RALN, RLTLN, LALN, and LLTLN were measured at all time points (Fig. 9a). No changes were observed in the weight of RALN and RLTLN during the first 4 h post-QD administration (3.20±0.98 mg for RALN and 2.57±0.40 mg for RLTLN, respectively, at 4 h) and were not different from controls ($p>0.05$). Right LN weights started to significantly increase at 24 h post-injection ($p<0.05$; Fig. 9a). For example, 10 days after QD injection, RALN and RLTLN weights were 8.59±0.595 and 7.59±2.20 mg, respectively (Fig. 9a).

H&E colorations of LN sections have revealed the presence of inflammation sites (light areas) in the two right LNs 10 days after QD delivery but not in left and control LNs (Fig. 9b). These signs of inflammation included numerous polynuclears, some histiocytes, and vacuoles of digestion in studied areas (Fig. 9c).

Discussion

QDs show rapid uptake in RALN and RLTLN after s.c. injection in mice, consistently with previous reports [27, 28, 33, 42, 43]. Both right LNs are readily detected as early as 5 min post-injection, using a very short CCD exposure time (10 ms). RALN and RLTLN show similar QD accumulation profiles assessed by i*n vivo* fluorescence or ICP–MS (cadmium concentration; Figs. 4 and 6a). Indeed, a very good correlation between these two detection techniques was highlighted by statistical analyses with a correlation coefficient of 0.89 and 0.81 for RALN and RLTLN, respectively (Fig. 8). We note, however, that stronger *in vivo* fluorescence signals were observed in RALN compared to RLTLN at all times whereas QD concentrations measured by ICP–MS are equivalent in these two LNs (Figs. 4 and 6a). This could be explained by the fact that LTLNs are deeper in the tissue than ALNs, which are just under the skin. The appearance of deep structures is significantly blurred in *in vivo* fluorescence imaging, and the signal detected from them is significantly attenuated as a function of structure depth [44, 45].

QD accumulation in RALN at 24 h post-delivery corresponds to 1.22% ID (Fig. 7b), as measured by ICP–MS, a result comparable with our previous study [43] in which accumulation of red-emitting QDs in RALN was performed by fluorescence measurements (1.24% ID at 24 h) and with Gopee's group [33] who found 1.07% ID in LNs 24 h after QD administration. RLTLN, which is considered as the second LN in the mouse axillary chain, also shows QD accumulation as early as 5 min after their delivery and display % ID values similar to RALN from 24 h for up to 10 days (Fig. 7b). These results are in agreement with Kobayashi's and Hama's studies [27, 28] which have shown lymphatic communication between ALN and LTLN after s.c. injection in the anterior paw of mice with QDs and NIR dyes, respectively. Maximum % ID in RALN and RLTLN

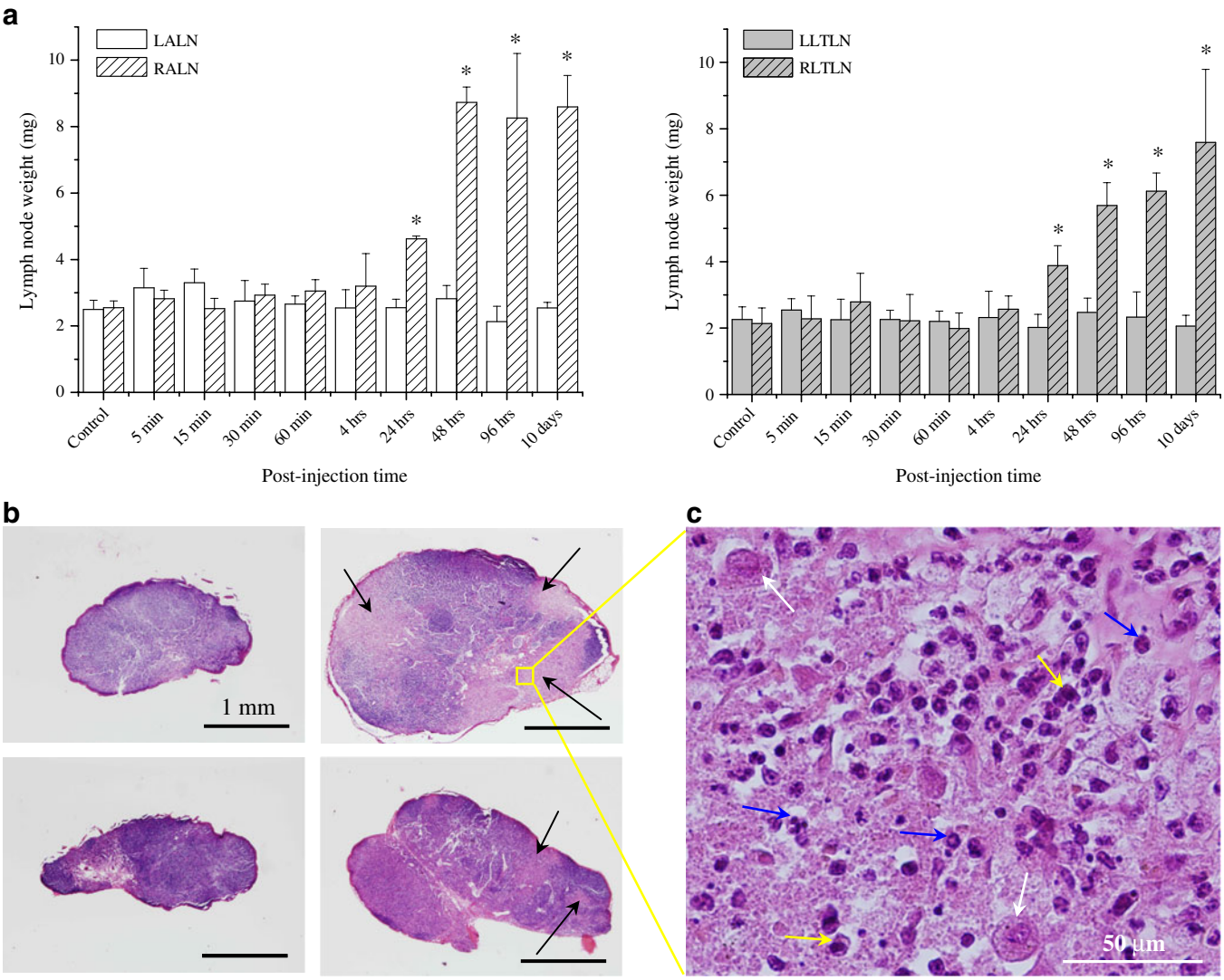

Fig. 9. Weight and histology of LNs after s.c. PBS (control) or QD injection (20 pmol). **a** Weight evolution of LN functions of time after PBS or QD delivery: *left panel* corresponds to ALNs and *right panel* to LTLNs. Data are mean ± SD ($n=3$ per group) and values marked with an *asterisk* were significantly different from control ($p<0.05$). **b** Histology of LN sections 10 days after product injection: control RALN (*upper left*), control RLTLN (*lower left*), RALN injected with QDs (*upper right*), and RLTLN injected with QDs (*lower right*). The *black arrows* indicate inflammation areas (*light site*). Magnification is ×25 and black scale corresponds to 1 mm. **c** Zoom of an inflammation area from RALN, 10 days after QD injection. Many polynuclears have been visualized but only some have been indicated with *blue arrows*. In the field of view, histiocytes (*yellow arrows*) and also vacuoles of digestion (*white arrows*) were observed. Magnification is ×400 and white scale corresponds to 50 µm.

was detected 4 h after QD injection and are followed by a plateau for the rest of the observation period (Fig. 7b). These results are consistent with the size of QDs (HD of 22 nm) since small particles (<10 nm) can rapidly pass the first LN without being retained, whereas larger particles (>100 nm) are trapped in the first LN, without possessing specific binding affinity to lymphatic vessels or LNs [46]. As a consequence, ideal lymph tracers that would both be efficiently retained and able to pass through the first LN must have a diameter comprised between 10 and 100 nm to fulfill both conditions. We observe that, although % ID in right LNs remains constant between 4 h and 10 days after QD delivery, cadmium concentrations per gram of tissue decrease (Figs. 6a and 7b). These observations can be explained by the increase in weight and volume of RALN and RLTLN from 24 h post-injection, reaching 2.7 times the weight of control LNs after 10 days (Fig. 9a, b).

QDs are remarkable tools for biomedical purposes, but they remain potentially toxic for living organisms. This toxicity is mainly due to the release of cadmium ions in biological environments, caused by deterioration and oxidation of QDs in the body [16, 17]. These heavy metal ions can also lead to the formation of reactive oxygen species that induce oxidative stress [47], particularly after a long-term exposure to QDs. Many *in vitro* toxicity studies of QDs have been realized [48–50] but only a few *in vivo* works have been performed. In our study, 10 days after QD injection, no signs of toxicity have been observed in living mice. Indeed,

body weight of mice was unchanged during the course of the study, no signs of abnormal motivity behavior were noticed, and no signs of dehydratation were registered. However, weight of removed right LNs had increased in QD-injected animals compared to control PBS-injected animals (Fig. 9a). Histological sections of LNs have shown inflammation of RALN and RLTLN in injected mice, revealing acute local toxicity of QDs without however any inflammation signs in the LALN, LLTLN, and control LNs (Fig. 9b, c). We attribute this difference to an effect of concentration, with QD doses corresponding to about 300 μg of cadmium/g provoking immunity reactions in LNs and smaller doses of about 30 μg of cadmium/g remaining without effects (Fig. 6a). This contrasts with results from previous studies using NIR dyes labeled with immunoglobulin G where no signs of inflammation were observed in LNs 7 days after injection [42]. Detailed assessment of QD toxicity in other organs was not performed in our work; hence, potential toxicity of QDs in these organs has not been demonstrated. Very recently, some QD toxicity has been reported in animals, showing for example pulmonary inflammation [51] or profound changes in mitochondria [36]. Several ways can be explored to limit QD toxicity, such as avoiding the use of heavy metals or design of surface chemistries allowing their complete elimination from the body, but *in fine* the QDs toxicity will strongly depend on the QDs biodistribution and concentration in the major organs. Knowledge of this biodistribution is therefore crucial for estimating the potential QDs toxicity.

We investigated the elimination of our QDs from the body by feces and urine. During 10 days of observation, QDs were not cleared from the body neither by urine nor feces (data not shown), suggesting that QDs are sequestered *in vivo*. Many authors have found that QDs were eliminated, albeit not completely, via urine and feces after intravenous (i.v.) [31, 35, 36, 52–55] or intranasal [56] injection. Other studies were similar to ours, and have shown that QDs were sequestrated in different organs and not cleared [31, 32, 34, 43]. Recent studies suggested that elimination by urine is strongly size dependent, with a maximum HD of about 5.5 nm for efficient clearance [53].

Increase in the blood cadmium concentration (plasma and blood cells) is detected as early as 5 min after QD injection (Fig. 6c), which suggests that QDs can enter blood vessels immediately after s.c. injection. This penetration could be either due to passive diffusion caused by concentration gradient between the different compartments or by leaking from lymphatic vessels into the blood network, considering that blood and lymphatic systems are intimately connected at the LNs. Four hours after QD administration, the cadmium concentration in blood starts to decrease due to progressive capture by various organs. This blood kinetics is different from that reported in other biodistribution studies, certainly due to differences in the QD delivery mode. Most QD biodistribution studies were performed after i.v. injection and show a rapid decrease of the blood QD concentration (typically by a factor 3 or 4 at 24 h compared to 1 h post-injection) and a total QD clearance from the blood after some days [34, 36, 37].

No *ex vivo* or *in vivo* fluorescence signals were observed in organs after 10 days post-injection compared to control organs. However, the presence of QDs is revealed by ICP–MS in most organs after injection. We attribute this difference to the lack of sensitivity of NIR imaging that hinders detection of very low QD concentrations in organs (0.04–13 μg/g of cadmium corresponding to 0.01–3.4 pmol/g of QDs).

Liver is the organ of the reticuloendothelial system with the higher QD concentrations after s.c. injection. These correspond to approximately 1.1%, 10.3%, and 15.4% ID at 1 h, 24 h, and 10 days post-delivery, respectively (Fig. 7a). This accumulation is much lower than that observed after QD i.v. injection [32, 34, 37, 53, 57]. For example, Fisher *et al.* [32] have found 36% ID in the liver 90 min after i.v. injection of QDs with a HD of 25 nm (lysine modified coating) and 100% ID post-injection in rats of biggest QDs with an HD of 80 nm (lysine modified and bovine serum albumin coating) by inductively coupled plasma–atomic emission spectroscopy (ICP–AES) analysis. Similarly, Soo Choi and co-workers [53] have investigated the distribution of ^{64}Cu-radiolabeled QDs by micro-positron emission tomography (microPET) and have shown that the fraction of small QDs (HD of 4.36 nm) in the liver at 4 h post-injection corresponded to 4% ID, but that this quantity increased to 28% ID with larger QDs (HD of 8.65 nm). Such differences in QD uptake in the liver can be explained by several factors including injection route and QD size and surface chemistry. In particular, the uptake of our QDs by the liver may be slowed down by the presence of PEG on its surface, as was observed in other studies [54, 55].

Overall, these results provide useful guidelines for use of QDs for SLN mapping by NIR fluorescence imaging. Efficient detection of regional LNs is achieved only a few minutes after s.c. injection.

Even though the QD concentration in the LNs still increases for up to 4 h post-injection, resection of the tumoral injection site and the SLN should ideally be performed during the first 15–30 min after injection to minimize QD leakage into the organism. At these early times, QD concentrations in the major organs remain very low, more than a hundred times lower than at the injection site or in the regional LNs. Since the SLN were readily detected in our configuration with only 10 ms of CCD exposure time, we can expect that the QD injected dose can be significantly reduced, so that the QD dose left in the body after the surgical act could be reduced well below toxicity concentrations. Investigations in this direction are in progress in our laboratory.

Conclusion

In conclusion, we have demonstrated that QD-based NIR fluorescence imaging can be used to very efficiently localize regional draining LNs *in vivo* as early as 5 min after s.c. injection in mice. Moreover, unlike other tracers, QDs remain trapped in these LNs during several days. Indeed,

in SLNB, it is recommended to inject radiocolloid the day before surgery to allow its migration to SLN followed by administration of physiologic dye in per-operative 5–10 min before SLN mapping. This short delay for physiological dye is related to its small size, and as a matter of fact it diffuses in all lymphatic system. Thus, rapid accumulation of QDs in regional LNs detected by non-invasive NIR fluorescence imaging system offers an exciting opportunity to track lymphatic flow in real time and guide their nodal dissection after a single QD injection and allows a rapid per-operative complete procedure.

This optical technique can also provide information about the kinetics of QD accumulation in specific regional LNs in the same animal, but fails to compare the relative QD concentration between different LNs or to detect low QD concentrations in organs. We determined the whole-body QD biodistribution by ICP–MS for 10 days after injection and provide guidelines for the use of QDs for non-invasive fluorescence detection of superficial LNs in a clinical setting.

Acknowledgements. This work was supported by the Institut National du Cancer (INCa), the Comités départementaux (54, 57) of the Ligue Contre le Cancer, the Ligue Nationale Contre le Cancer, and the Région Lorraine.

References

1. Marchal F, Rauch P, Morel O et al (2006) Results of preoperative lymphoscintigraphy for breast cancer are predictive of identification of axillary sentinel lymph nodes. World J Surg 30:55–62
2. Rovera F, Frattini F, Marelli M et al (2008) Axillary sentinel lymph node biopsy: an overview. Int J Surg 6 Suppl:S109–112
3. Ferrari A, Rovera F, Dionigi P et al (2006) Sentinel lymph node biopsy as the new standard of care in the surgical treatment for breast cancer. Expert Rev Anticancer Ther 6:1503–1515
4. Noguchi M (2002) Sentinel lymph node biopsy and breast cancer. Br J Surg 89:21–34
5. Wilke LG, McCall LM, Posther KE et al (2006) Surgical complications associated with sentinel lymph node biopsy: results from a prospective international cooperative group trial. Ann Surg Oncol 13:491–500
6. Sato K (2007) Current technical overviews of sentinel lymph node biopsy for breast cancer. Breast Cancer 14:354–361
7. Sato K, Shigenaga R, Ueda S, Shigekawa T, Krag DN (2007) Sentinel lymph node biopsy for breast cancer. J Surg Oncol 96:322–329
8. Montgomery LL, Thorne AC, Van Zee KJ et al (2002) Isosulfan blue dye reactions during sentinel lymph node mapping for breast cancer. Anesth Analg 95:385–388
9. Scherer K, Studer W, Figueiredo V, Bircher AJ (2006) Anaphylaxis to isosulfan blue and cross-reactivity to patent blue V: case report and review of the nomenclature of vital blue dyes. Ann Allergy Asthma Immunol 96:497–500
10. Mujtaba B, Adenaike M, Yaganti V, Mujtaba N, Jain D (2007) Anaphylactic reaction to Tc-99 m sestamibi (Cardiolite) during pharmacologic myocardial perfusion imaging. J Nucl Cardiol 14:256–258
11. Chicken DW, Mansouri R, Ell PJ, Keshtgar MR (2007) Allergy to technetium-labelled nanocolloidal albumin for sentinel node identification. Ann R Coll Surg Engl 89:W12–W13
12. Kaleya RN, Heckman JT, Most M, Zager JS (2005) Lymphatic mapping and sentinel node biopsy: a surgical perspective. Semin Nucl Med 35:129–134
13. Murray CB, Norris DG, Bawendi MG (1993) Synthesis and characterization of nearly monodisperse CdE (E-S, Se, Te) semiconductor nanocrystallites. J Am Chem Soc 115:8706–8715
14. Alivisatos AP (1996) Semiconductor clusters, nanocrystals, and quantum dots. Science 271:933–937
15. Bruchez M Jr, Moronne M, Gin P, Weiss S, Alivisatos AP (1998) Semiconductor nanocrystals as fluorescent biological labels. Science 281:2013–2016
16. Ipe BI, Lehnig M, Niemeyer CM (2005) On the generation of free radical species from quantum dots. Small 1:706–709
17. Derfus A, Chan WCW, Bhatia S (2004) Probing the cytotoxicity of CdSe quantum dots with surface modification. Nano Lett 4:11–18
18. Yu WW, Chang E, Drezek R, Colvin VL (2006) Water-soluble quantum dots for biomedical applications. Biochem Biophys Res Commun 348:781–786
19. Carion O, Mahler B, Pons T, Dubertret B (2007) Synthesis, encapsulation, purification and coupling of single quantum dots in phospholipid micelles for their use in cellular and *in vivo* imaging. Nat Protoc 2:2383–2390
20. Pons T, Lequeux N, Mahler B et al (2009) Synthesis of near-infrared-emitting, water-soluble CdTeSe/CdZnS core/shell quantum dots. Chem Mater 21(8):1418–1424
21. Soltesz EG, Kim S, Kim SW et al (2006) Sentinel lymph node mapping of the gastrointestinal tract by using invisible light. Ann Surg Oncol 13:386–396
22. Parungo CP, Colson YL, Kim SW et al (2005) Sentinel lymph node mapping of the pleural space. Chest 127:1799–1804
23. Soltesz EG, Kim S, Laurence RG et al (2005) Intraoperative sentinel lymph node mapping of the lung using near-infrared fluorescent quantum dots. Ann Thorac Surg 79:269–277
24. Parungo CP, Ohnishi S, Kim SW et al (2005) Intraoperative identification of esophageal sentinel lymph nodes with near-infrared fluorescence imaging. J Thorac Cardiovasc Surg 129:844–850
25. Tanaka E, Choi HS, Fujii H, Bawendi MG, Frangioni JV (2006) Image-guided oncologic surgery using invisible light: completed pre-clinical development for sentinel lymph node mapping. Ann Surg Oncol 13:1671–1681
26. Kim S, Lim YT, Soltesz EG et al (2004) Near-infrared fluorescent type II quantum dots for sentinel lymph node mapping. Nat Biotechnol 22:93–97
27. Kobayashi H, Hama Y, Koyama Y et al (2007) Simultaneous Multicolor Imaging of Five Different Lymphatic Basins Using Quantum Dots. Nano Lett 7:1711–1716
28. Hama Y, Koyama Y, Urano Y, Choyke PL, Kobayashi H (2007) Simultaneous two-color spectral fluorescence lymphangiography with near infrared quantum dots to map two lymphatic flows from the breast and the upper extremity. Breast Cancer Res Treat 103:23–28
29. Ballou B, Ernst LA, Andreko S et al (2007) Sentinel lymph node imaging using quantum dots in mouse tumor models. Bioconjug Chem 18:389–396
30. Knapp DW, Adams LG, Degrand AM et al (2007) Sentinel lymph node mapping of invasive urinary bladder cancer in animal models using invisible light. Eur Urol 52:1700–1708
31. Chen Z, Chen H, Meng H et al (2008) Bio-distribution and metabolic paths of silica coated CdSeS quantum dots. Toxicol Appl Pharmacol 230:364–371
32. Fischer H, Liu L, Pang K, Chan W (2006) Pharmacokinetics of nanoscale quantum dots: *in vivo* distribution, sequestration, and clearance in the rat. Adv Funct Mater 16:1299–1305
33. Gopee NV, Roberts DW, Webb P et al (2007) Migration of intradermally injected quantum dots to sentinel organs in mice. Toxicol Sci 98:249–257
34. Yang RS, Chang LW, Wu JP et al (2007) Persistent tissue kinetics and redistribution of nanoparticles, quantum dot 705, in Mice: ICP–MS quantitative assessment. Environ Health Perspect 115:1339–1343
35. Duconge F, Pons T, Pestourie C et al (2008) Fluorine-18-Labeled phospholipid quantum dot micelles for *in vivo* multimodal imaging from whole body to cellular scales. Bioconjug Chem 19:1921–1926
36. Lin P, Chen JW, Chang LW et al (2008) Computational and ultrastructural toxicology of a nanoparticle, quantum dot 705, in mice. Environ Sci Technol 42:6264–6270
37. Geys J, Nemmar A, Verbeken E et al (2008) Acute toxicity and prothrombotic effects of quantum dots: impact of surface charge. Environ Health Perspect 116:1607–1613
38. Daou TJ, Li L, Reiss P, Josserand V, Texier I (2009) Effect of poly (ethylene glycol) length on the *in vivo* behavior of coated quantum dots. Langmuir 25(5):3040–3044
39. Kostarelos K (2009) Tumor targeting of functionalized quantum dot-liposome hybrids by intravenous administration. Mol Pharma 6(2):520–530
40. Pic E, Bezdetnaya L, Guillemin F, Marchal F (2009) Quantification techniques and biodistribution of semiconductor quantum dots. Anti-cancer Agents Med Chem 9:295–303

41. Dubertret B, Skourides P, Norris DJ et al (2002) *In vivo* imaging of quantum dots encapsulated in phospholipid micelles. Science 298:1759–1762
42. Hama Y, Koyama Y, Urano Y, Choyke PL, Kobayashi H (2007) Two-color lymphatic mapping using Ig-conjugated near infrared optical probes. J Invest Dermatol 127:2351–2356
43. Robe A, Pic E, Lassalle HP et al (2008) Quantum dots in axillary lymph node mapping: biodistribution study in healthy mice. BMC Cancer 8:111
44. Ntziachristos V, Bremer C, Weissleder R (2003) Fluorescence imaging with near-infrared light: new technological advances that enable *in vivo* molecular imaging. Eur Radiol 13:195–208
45. Ntziachristos V, Ripoll J, Wang LV, Weissleder R (2005) Looking and listening to light: the evolution of whole-body photonic imaging. Nat Biotechnol 23:313–320
46. Tanis PJ, Nieweg OE, Valdes Olmos RA, Kroon BB (2001) Anatomy and physiology of lymphatic drainage of the breast from the perspective of sentinel node biopsy. J Am Coll Surg 192:399–409
47. Maysinger D, Behrendt M, Lalancette-Hebert M, Kriz J (2007) Real-time imaging of astrocyte response to quantum dots: *in vivo* screening model system for biocompatibility of nanoparticles. Nano Lett 7:2513–2520
48. Clift MJ, Rothen-Rutishauser B, Brown DM et al (2008) The impact of different nanoparticle surface chemistry and size on uptake and toxicity in a murine macrophage cell line. Toxicol Appl Pharmacol 232:418–427
49. Wang L, Nagesha DK, Selvarasah S, Dokmeci MR, Carrier RL (2008) Toxicity of CdSe Nanoparticles in Caco-2 Cell Cultures. J Nanobiotechnol 6:11
50. Stern ST, Zolnik BS, McLeland CB et al (2008) Induction of autophagy in porcine kidney cells by quantum dots: a common cellular response to nanomaterials? Toxicol Sci 106:140–152
51. Jacobsen NR, Moller P, Jensen KA et al (2009) Lung inflammation and genotoxicity following pulmonary exposure to nanoparticles in ApoE−/− mice. Part Fibre Toxicol 6:2
52. Diagaradjane P, Orenstein-Cardona JM, Colon-Casasnovas EN et al (2008) Imaging epidermal growth factor receptor expression *in vivo*: pharmacokinetic and biodistribution characterization of a bioconjugated quantum dot nanoprobe. Clin Cancer Res 14:731–741
53. Soo Choi H, Liu W, Misra P et al (2007) Renal clearance of quantum dots. Nat Biotechnol 25:1165–1170
54. Schipper ML, Cheng Z, Lee SW et al (2007) microPET-based biodistribution of quantum dots in living mice. J Nucl Med 48:1511–1518
55. Schipper ML, Iyer G, Koh AL et al (2009) Particle size, surface coating, and PEGylation influence the biodistribution of quantum dots in living mice. Small 5:126–134
56. Gao X, Chen J, Chen J et al (2008) Quantum dots bearing lectin-functionalized nanoparticles as a platform for *in vivo* brain imaging. Bioconjug Chem 19:2189–2195
57. Chen K, Li ZB, Wang H, Cai W, Chen X (2008) Dual-modality optical and positron emission tomography imaging of vascular endothelial growth factor receptor on tumor vasculature using quantum dots. Eur J Nucl Med Mol Imaging 35:2235–2244